tvst

https://doi.org/10.1167/tvst.8.3.18

Article

Photothermal Optical Coherence Tomography of Anti-Angiogenic Treatment in the Mouse Retina Using Gold Nanorods as Contrast Agents

Andrew Y. Gordon[1], Maryse Lapierre-Landry[2,3], Melissa C. Skala[3,4], and John S. Penn[1,5]

[1] Department of Molecular Physiology and Biophysics, Vanderbilt University Medical Center, Nashville, TN, USA
[2] Department of Biomedical Engineering, Vanderbilt University, Nashville, TN, USA
[3] Morgridge Institute for Research, Madison, WI, USA
[4] Department of Biomedical Engineering, University of Wisconsin Madison, Madison, WI, USA
[5] Department of Ophthalmology and Visual Sciences, Vanderbilt University Medical Center, Nashville, TN, USA

Correspondence: Andrew Y. Gordon, Vanderbilt University Medical Center, Molecular Physiology and Biophysics, Medical Center North, 1161 21st Avenue S, Nashville, TN 37232, USA. e-mail: andrew.y.gordon@vanderbilt.edu

Received: 17 September 2018
Accepted: 28 February 2019
Published: 14 May 2019

Keywords: optical coherence tomography; gold nanorods; laser-induced choroidal neovascularization; mice

Citation: Gordon AY, Lapierre-Landry M, Skala MC, Penn JS. Photothermal optical coherence tomography of anti-angiogenic treatment in the mouse retina using gold nanorods as contrast agents. Trans Vis Sci Tech. 2019;8(3):18, https://doi.org/10.1167/tvst.8.3.18

Purpose: Optical coherence tomography (OCT) is widely used for ocular imaging in clinical and research settings. OCT natively provides structural information based on the reflectivity of the tissues it images. We demonstrate the utility of photothermal OCT (PTOCT) imaging of gold nanorods (GNR) in the mouse retina in vivo in the laser-induced choroidal neovascularization (LCNV) model to provide additional image contrast within the lesion.

Methods: Wild-type C57BL/6 mice were imaged following the intravenous injection of ICAM2-targeted or untargeted GNR. Mice were also imaged following the injection of ICAM2-targeted GNR with or without the additional ocular delivery of a neutralizing monoclonal anti-vascular endothelial growth factor (anti-VEGF) antibody.

Results: Mice cohorts injected with untargeted or ICAM2-targeted GNR demonstrated increased lesion-associated photothermal signal during subsequent imaging relative to phosphate-buffered saline (PBS)-injected controls. Additionally, intravitreal injection of anti-VEGF antibody caused a detectable reduction in the extent of anatomic laser damage and lesion-associated photothermal signal density in mice treated in the LCNV model and injected with ICAM2-targeted GNR.

Conclusions: These experiments demonstrate the ability of PTOCT imaging of GNR to detect anti-VEGF-induced changes in the mouse retina using the LCNV model.

Translational Relevance: This study shows that PTOCT imaging of GNR in the LCNV model can be used to detect clinically relevant, anti-VEGF-induced changes that are not visible using standard OCT systems. In the future this technology could be used to aid in early detection of disease, monitoring disease progress, and assessing its response to therapies.

Introduction

Optical coherence tomography (OCT) provides high resolution images of tissue structure.[1] The most common clinical application of OCT is in the eye, and OCT is particularly effective at imaging retinal disease including age-related macular degeneration (AMD), diabetic retinopathy (DR), and glaucoma.[2–5] Additionally, in research settings, OCT has been used to image a wide variety of other tissues, including a number of tumor types, the skin, and skin malignancies. OCT endoscopy has been used to image atherosclerotic plaques and polypoid lesions in the colon.[6] The major advantage of OCT over other clinically relevant imaging modalities, like fluorescence imaging, is that it is inherently three-dimensional. Clinicians can therefore apply its micron-scale resolving power to easily image structural changes that have a significant component of growth perpen-

dicular to the layers of the retina. These directions of growth are particularly pertinent for retinal vascular disease.

Despite the clinical utility and broad research applicability of OCT, currently it can only be used to gather information relevant to pathologies that have progressed to a point where they cause detectable morphological changes in tissue. This is particularly pertinent in retinal imaging where loss of visual acuity can occur prior to, or concurrent with, detectable changes in tissue reflectivity or morphology.[7–9] This difficulty in achieving early detection of incipient retinal vascular disease is a major clinical problem because it narrows the window of time during which retinal disease can be detected and therefore treated without some degree of vision loss. Since retinal disease can cause changes at a cellular level prior to causing clinically detectable pathology, detection of these changes is one of the major goals of molecular imaging using OCT.

Research in OCT aims to achieve this goal by combining the native capabilities of OCT with additional technologies that can allow researchers to collect more information about molecular expression in relevant tissue without sacrificing the high resolution consistent with OCT imaging.[10] The difficulty with detecting molecular changes using OCT is that such changes are not generally detectable using simple measures of tissue reflectivity, particularly in the relatively heterogeneous tissue of the retina. So, researchers have used adjuncts to OCT that can target these changes while being compatible with OCT systems. This has led to a variety of exogenous imaging adjuvants that can be observed using modified OCT systems. Approaches have been varied, including the use of ferromagnetic particles with magnetomotive OCT, dyes with pump-probe OCT, and gold nanoparticles with spectral fractionation, hyperspectral, diffusion-sensitive, and photothermal OCT (PTOCT) among others.[11–18] Despite this considerable research effort, to date none of these OCT-based technologies have been used to achieve molecular imaging in the heterogeneous tissue of the retina in vivo, which has limited their clinical potential.

Gold nanoparticles remain an excellent candidate for clinical translation because they are versatile, tunable optical absorbers, and these properties are important for exogenous contrast agents used in OCT imaging.[19] Here we use molecularly targeted gold nanorods (GNR) in conjunction with PTOCT to generate contrast in the mouse retina. PTOCT operates by heating a contrast agent using an amplitude-modulated monochromatic laser. This localized heating changes the optical path length of light passing through tissue surrounding the contrast agent which is then detected in the OCT phase signal.[15] GNR are used as a contrast agent for PTOCT because they have a high absorption coefficient at the wavelength used for heating by the PTOCT system.[20,21] Additionally, GNR can be readily functionalized with specific antibodies that cause them to bind to specific antigens expressed on targeted cells.[22–25] It has been demonstrated that appropriately tuned GNR can be detected using PTOCT in tissue in situ as well as in vivo.[26–28] The combined use of GNR and PTOCT potentially allows for the imaging of molecular expression at a cellular level.

To generate an appropriate target for molecular imaging in vivo, we use the laser-induced choroidal neovascularization (LCNV) model in the mouse, which is a model commonly used to study neovascular or "wet" AMD.[29–31] An ultraviolet-range laser is targeted to the retinal pigmented epithelium (RPE) layer of the outer retina and, when fired, the light energy is absorbed by the pigment in this layer and released as heat, which rapidly degrades the integrity of the RPE and Bruch's membrane, creating a breach in these tissues. Collocational with this injury, there is the proliferation of endothelial cells derived from the choroidal vasculature and this growth invades the subretinal space.[32,33] RPE cells are concentrated at the borders of the injury at this time. The lesion caused by laser damage peaks in size 7 days after laser injury, with the presence of newly formed vessels extending into the subretinal space along with a high concentration of RPE cells. After day 7, the lesion size plateaus and then begins to spontaneously resolve, though the lesion can persist for more than 4 weeks.[34] This lesion is localized to the area surrounding the laser injury, and can be imaged using OCT.[35] Previously published studies suggest that the vast majority of lesions of anatomical damage formed in the LCNV model contain choroidal neovascularization.[36] Several antibody-targetable surface ligands are upregulated in these lesions, the most important for this study being CD102/ICAM2, which is a constitutively expressed on vascular endothelial cells.[37–43]

In our previous publication, we demonstrate the ability of PTOCT to image untargeted, passively accumulated GNR as exogenous contrast in vivo.[16] In this paper, we assess the utility of PTOCT imaging of molecularly targeted GNR to achieve high-resolution in vivo imaging of tissue protein expression in the

mouse retina. To accomplish this, we intravenously deliver ICAM2-targeted GNR to mice treated with LCNV, using untargeted GNR or phosphate-buffered saline (PBS) used as controls. We then image the anatomic lesion caused by laser damage using a custom PTOCT system and compare the lesion-associated photothermal signal in mice injected with targeted GNR versus our two controls to assess for successful imaging of molecularly targeted GNR in vivo. Additionally, to test the ability of our imaging technologies to achieve clinically relevant molecular imaging, we report results from an experiment in which ICAM2-targeted GNR are intravenously injected in LCNV mice with the additional intravitreal injection of a neutralizing anti-vascular endothelial growth factor (anti-VEGF) antibody, using intravitreal PBS injections as a control. As VEGF signaling is an important driver of neovascularization in LCNV lesions, anti-VEGF treatment is expected to reduce the proliferation of vascular endothelial cells in these lesions and, consequently, overall lesion volume, thereby causing reduced lesion-associated signal from ICAM2-targeted GNR.[44–46] This experiment allows us to investigate the utility of our imaging technology to detect physiological changes in vivo. To the best of our knowledge both the in vivo detection of molecularly targeted GNR in the retina and the use of GNR to report on changes in retinal lesions in vivo are novel applications of OCT-based imaging technology.

Methods

GNR Functionalization

All GNR referenced in this paper have a peak absorption of 750 nm, with dimensions of 10 nm by 35 nm. They are commercially available with a covalently attached carboxyl moiety (C12-10/750-TC-50; Nanopartz, Loveland, CO). We functionalized these GNR with one of two different antibodies to create the targeted and untargeted GNR employed in this study. The first antibody was a rat IgG with no known reactivity to murine antigens (Thermo Fisher Scientific, Waltham, MA); this was our "untargeted" control antibody. The second antibody was a rat anti-ICAM2 antibody (Thermo Fisher Scientific), which was our "targeted" antibody. Surface functionalization of these GNR with the appropriate antibodies (untargeted or anti-ICAM2) was achieved in a directed fashion. We performed an ethyl-3-(3-dimethylaminopropyl) carbodiimide (EDC) (Thermo Fisher Scientific) crosslinking reaction with the addition of N-hydroxysulfosuccinimide (sulfo-NHS) (Thermo Fisher Scientific) to the reaction mixture to improve our reaction yield. 10^{12} GNR were mixed with EDC and sulfo-NHS at 10-fold and 25-fold molar concentrations relative to surface carboxyl groups in 1 mL deionized water. This mixture was allowed to react for 2 hours at room temperature with a magnetic stirring rod used to facilitate continuous mixing before purification of the GNR via centrifugation at 18,000*g* for 45 minutes followed by resuspension in deionized water. The appropriate untargeted or anti-ICAM2 antibody was then added to the resuspended GNR at a 50-fold molar concentration relative to surface carboxyl moieties on the GNR. This mixture was allowed to react for 2 hours at room temperature with a magnetic stirring rod to facilitate mixing. The final GNR product was purified via three rounds of centrifugation at 18,000*g* for 45 minutes and resuspension in 1 mL isotonic PBS. A transmission electron microscope (TEM) was used to image GNR after functionalization to ensure that they maintained the appropriate morphology during the process (Fig. 1a).

Drug Delivery, Lasering, and Imaging

Male C57BL/6 mice aged 8 to 10 weeks were used in all in vivo imaging experiments. For all imaging procedures, animals were anesthetized using continuous isoflurane administration (2%–5%) in air in a box or via nose cone. For procedures involving laser photocoagulation or drug delivery via any route, anesthesia was accomplished using the intraperitoneal injection of 3.7 mL/kg body weight of a cocktail containing 13.2 mg/mL ketamine and 1.5 mg/mL xylazine in sterile water. Mice were allowed to recover following anesthesia on heating blankets. Animal treatments followed all requirements of the Vanderbilt University Institutional Animal Care and Use Committee and adhered to the ARVO Statement for the Use of Animals in Ophthalmic and Vision Research.

In our experiments, two routes of drug delivery were used. The first route, used to deliver GNR and appropriate controls systemically, was a tail-vein injection. For these injections, 100 μL of a GNR solution or PBS was administered. Intravenous injections were performed 8 hours prior to imaging. In this study, one randomly selected lesion from 21 mice was assessed in our control cohort. Both GNR-injected cohorts involved the study of one lesion from 14 mice. Intravitreal injections were performed via

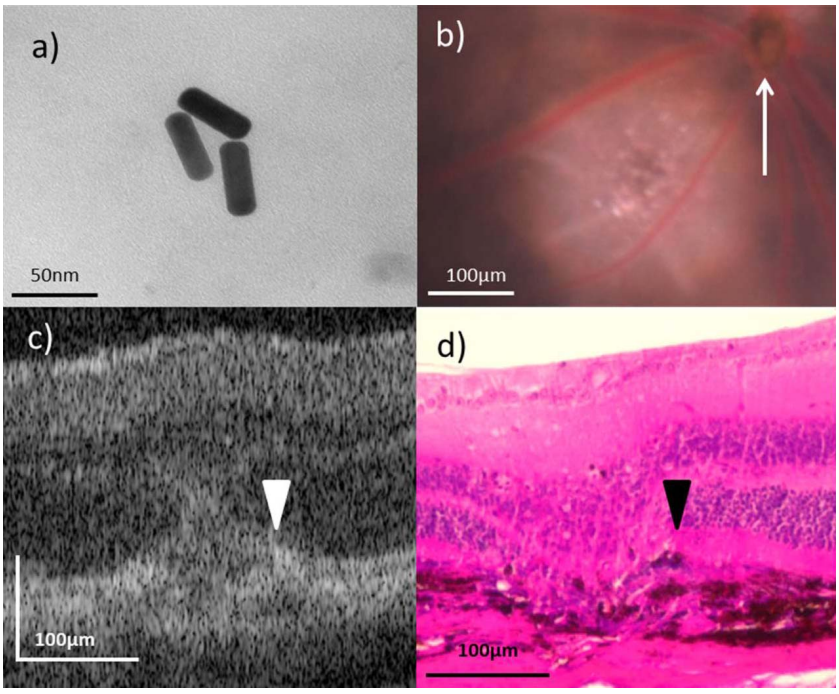

Figure 1. GNR functionalization and imaging. (a) Transmission electron micrographs of GNR demonstrating unaltered morphology following surface functionalization. (b) In vivo fundoscopy showing a day 5 LCNV lesion adjacent to the optic nerve head (*white arrow*). (c, d) Representative OCT in vivo and hematoxylin and eosin stained ex vivo images of day 5 LCNV lesions, with disrupted RPE (*white* and *black arrowheads*, respectively) present.

injection through the cornea of 2 µL anti-VEGF antibody (AF-493-NA; R&D Systems; Minneapolis, MN) solution in one eye of a given mouse, with a matched volume of PBS injected in the contralateral eye as a control. These intravitreal injections were performed immediately following laser photocoagulation. Single lesions from seven paired mouse eyes were assessed in this part of the study.

The laser photocoagulation required for the LCNV model was performed with a laser system (Carl Zeiss Meditec, Jena, Germany) utilizing a laser (Coherent, Santa Clara, CA) operating at 532 nm and 120 mW pulsed for 0.1 seconds. Ocular manipulation and fundus visualization were aided by the use of a microscope slide cover slip and a 2.5% hydroxypropyl methylcellulose solution. The spot size on the retina was 100 microns, and for each eye we attempted to generate four laser injuries centered equidistant from the optic nerve head with a space of approximately two optic disc diameters between the site of laser injury and the optic nerve head. In aiming the laser, we sought to avoid hitting major blood vessels. This approach consistently produced visible vapor bubbles following laser firing, an indication that Bruch's membrane was being ruptured. All in vivo imaging was performed 5 days following laser photocoagulation. Representative day 5 LCNV lesions imaged using the Micron IV imaging system (Phoenix Research Labs, Pleasanton, CA) in vivo via bright-light fundoscopy and our modified spectral-domain OCT system (Leica Microsystems, Inc., Buffalo Grove, IL) can be seen in Figures 1b and 1c.

We imaged day 5 LCNV lesions because, while vascular endothelial cells are present in the lesions by this point,[35] the RPE is still disrupted, as shown in Figure 1d. We felt this time point presented the best opportunity to capture GNR-generated photothermal signal while excluding the photothermal signal generated by RPE-associated melanin, a signal that we expected to be present based on results from our previously published studies.[16]

Instrumentation, Signal Analysis, and Image Correction

For a more thorough explanation of the PTOCT instrumentation, image collection protocols, and image corrections algorithms, please see our previously published work.[16] Briefly, a spectral-domain OCT system (Leica Microsystems, Inc.) was modified to allow for PTOCT imaging. The OCT system's

broadband light source was centered at 860 nm (40 nm bandwidth), while the additional laser used for photothermal imaging was centered at 750 nm with a power of 8 mW and amplitude-modulated by an acousto-optics modulator (Brimrose, Sparks, MD) at $f_0 = 500$ Hz (50% duty-cycle, square wave). Scan patterns were 700 repeated A-scans (M-scans) at each sample location, and 400 A-scans/B-scans. Collected data were processed using custom MATLAB code.[27] The data were first resampled from wavelength to wavenumber, dispersion compensated, and background subtracted. A Chirp Z transform was used to obtain the OCT magnitude and phase signal as a function of depth. The temporal derivative of the phase signal was then taken over time. A Fourier transform of the phase signal was performed to go from the time domain to the frequency domain. The amplitude of the peak at $f_0 = 500$ Hz minus the average amplitude of the signal at surrounding frequencies was taken as the PTOCT signal. The PTOCT signal is expressed as the change in the optical path length in the tissue due to the photothermal excitation in units of nanometers. Images were corrected for breathing artifacts associated with retinal imaging in live animals following an algorithm described in Guizar-Sicairos et al.[16,47] Once processed, data analysis was performed by hand-selecting the lesion of anatomic laser damage on individual B-scans that have been imaged in a given retina and calculating both the lesion volume and the lesion-associated PTOCT signal inside the selected volume by collating available B-scan measurements into volumes. Lesions were excluded from measurement if there were gross morphological anomalies on OCT, most commonly retinal detachment, and individual B-scans were excluded if the image quality was degraded to a point where photothermal signal measurement was infeasible. These volume measurements were then used to compute a photothermal signal density, defined as the PT signal divided by lesion volume. Selections were made to include the lesions but exclude the adjacent RPE layer, since the RPE layer contains melanin, which also produces a photothermal signal. Selections were made based on the OCT image while blinded to the PTOCT signal present in the lesion. Additional nonphotothermal OCT scans of lesions were used to estimate the extent of anatomic laser damage by measuring the size of the lesion on the B-scan with the maximum area of anatomic laser damage for a given set of scans, which is the lesion diameter.

Significance Tests

Significance testing was performed following consultation with the Vanderbilt University Center for Quantitative Sciences. For the three-armed control/untargeted/targeted GNR experiment, since some mice have both eyes imaged while some have only one eye imaged, a cluster analysis was performed to determine the statistical significance of differences in the means of our three cohorts. A Tukey analysis was performed following estimations of statistical fixed effects between the three cohorts using a linear mixed effect model. For the second set of experiments involving anti-VEGF injection in one eye and PBS injection in the other eye of the same mouse, given the paired nature of the experimental design and directional nature of the expected results, a 1-tailed Wilcoxon signed-rank analysis was used to test for significance of differences in lesion-associated photothermal signal, as well as in lesion size. In all cases a P-value ≤ 0.05 was considered significant.

Results

In Vivo Retinal PTOCT Imaging of Targeted and Untargeted GNR

C57BL/6 mice were treated in the LCNV model. Five days following lasering, the mice were intravenously injected with PBS, untargeted GNR, or ICAM2-targeted GNR via a tail vein injection. The injected GNR were allowed to circulate for 8 hours prior to imaging. We assessed these cohorts for lesion-associated photothermal signal. Our previous work shows that both RPE-associated melanin and the targeting-independent accumulation of GNR both generate some photothermal signal.[16] In the cohort injected with ICAM2-targeted GNR, we assessed for the presence of an additional targeting-dependent photothermal signal.

The graph in Figure 2a reports measurements of the photothermal signal density in lesions of anatomic laser damage imaged by our PTOCT system in all three experimental arms. In lesions of mice injected with PBS, there was an average photothermal density of 2.82 nm/pixel ($\pm$1.20 nm/pixel standard deviation, $n = 21$), which we will take as a baseline measurement. The photothermal signal was 1.49 times stronger than at baseline in mice injected with untargeted GNR (4.20 $\pm$ 1.74 nm/pixel, $n = 14$), and the signal was further increased to 1.73 times baseline in lesions of mice injected with ICAM2-targeted GNR (4.89 $\pm$

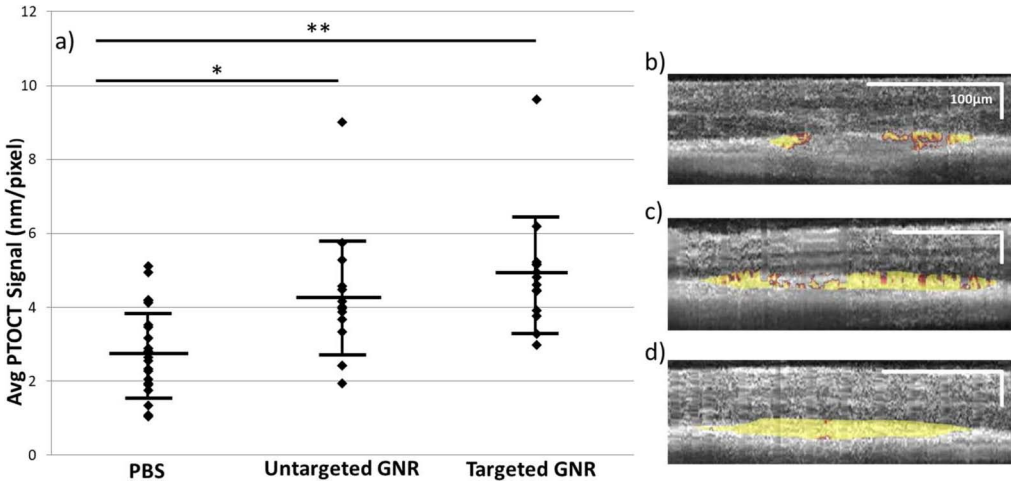

Figure 2. PTOCT of untargeted and targeted GNR in vivo. (a) Average PTOCT signal density for each cohort, with error bars representing standard error of the mean. There is a significant increase in this signal associated with both untargeted and targeted GNR injections versus PBS control. *$P \leq 0.05$; **$P \leq 0.001$. (b–d) Representative OCT B-scans of mice injected with PBS (b; $n = 21$ eyes), untargeted GNR (c; $n = 14$ eyes), and targeted GNR (d; $n = 14$ eyes), respectively, with lesion-associated photothermal signal overlaid in gold. Note the increased concentration of photothermal signal associated with passive accumulation of GNR in the lesions, and the greater increase associated with the injection of targeted GNR.

1.60 nm/pixel, $n = 14$). There is a statistically significant difference in reported lesion-associated photothermal density between the untargeted GNR and PBS cohorts, as well as between the targeted GNR and PBS cohorts. The difference between the untargeted and targeted GNR cohorts is not statistically significant, although there is a trend toward more signal in the targeted cohort, consistent with a molecular targeting effect. Representative OCT B-scans from each experimental group with overlaid photothermal signal (in gold) are shown in Figures 2b to 2d.

Alterations in Targeted GNR Accumulation Following Pharmaceutical Intervention

One of the goals of molecular imaging is to detect disease-associated changes that might indicate disease progression or response to therapy. To further assess the efficacy of this technology to achieve clinically relevant molecular imaging, we modified our experimental protocol to include the intravitreal injection of an anti-mouse-VEGF neutralizing antibody that should downregulate choroidal angiogenesis and thus the expression of ICAM2 in LCNV lesions while also reducing targeting-independent GNR accumulation. All mice in this experiment were treated in the LCNV model. Immediately following lasering, the mice were intravitreally injected with anti-VEGF antibody in one eye, and PBS in the other. Five days following lasering, they were intravenously injected with ICAM2-targeted GNR. PTOCT imaging was performed following 8 hours of GNR accumulation. Measurement of PTOCT signal density proceeded as in our previous experiment.

Confirmation of the effect of the anti-VEGF injections on the extent of anatomic laser damage is shown in Figure 3. The lesion diameters as measured using standard OCT B-scans are reported for the seven pairs of eyes used in this portion of the study. As shown in Figure 3a, in all cases the eye injected with anti-VEGF has a reduced lesion diameter, which is a statistically significant decrease. The mean of the measurements in the PBS-injected cohort is 7332 pixels (±1862 pixels standard deviation, $n = 7$), while for the anti-VEGF-injected cohort the mean is 5209 pixels (±1493 pixels, $n = 7$). This finding provides strong evidence that the anti-VEGF injections had an effect consistent with disruption of the VEGF signaling pathway in the LCNV model, which includes decreasing lesion volume, reduced endothelial cell concentration, and inhibition of vascular leakiness.[44,45,48–50] Figures 3b and 3c show representative OCT B-scans of lesions from both cohorts.

The results of PTOCT signal density measurements are shown in Figure 4. Intravitreal injection of anti-VEGF antibody caused a detectable reduction of photothermal signal density in mouse lesions of anatomic laser damage. Because each mouse had one eye injected intravitreally with PBS and one eye injected with anti-VEGF, a paired analysis was

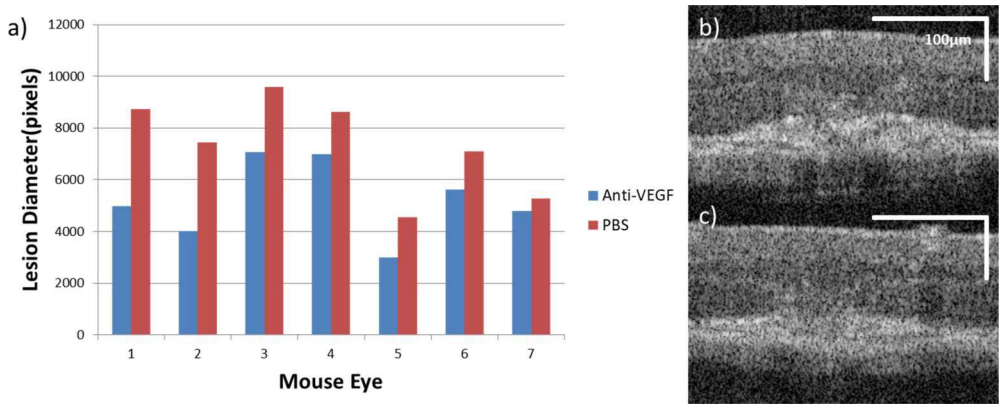

Figure 3. Estimates of lesion size with or without intravitreal anti-VEGF injection in vivo. (a) The lesion diameter from every eye in both experimental cohorts, paired by mouse ($n = 7$ mice). The results are ordered from greatest to least magnitude of difference. The statistical significance of the difference between the PBS and anti-VEGF eyes was assessed using a Wilcoxon signed-rank test. $W = 28$; $P \leq 0.05$. The OCT B-scans in (b, c) show representative lesions from mice intravitreally injected with PBS and anti-VEGF, respectively. Both images are from mouse 5.

performed. Figure 4a shows that of the seven pairs of eyes measured, there was reduced PTOCT signal density associated with anti-VEGF injections in six pairs. There is a statistically significant difference between the two experimental arms that demonstrates the detection of nonstructural, anti-VEGF-induced changes in the microenvironment in the lesions in vivo using PTOCT imaging of targeted GNR. The mean of the photothermal signal measurements in the PBS-injected cohort is 3.91 nm/pixel (±0.92 nm/pixel standard deviation, $n = 7$), while for the anti-VEGF-injected cohort the mean is 2.85 nm/pixel (±1.02 nm/pixel, $n = 7$). Figure 4b shows a representative OCT b-scan with lesion-associated PTOCT signal overlay from an anti-VEGF-injected eye, while Figure 4c shows the control eye of the same mouse.

Discussion

OCT is a powerful and widely used ocular imaging modality in both clinical and research settings. Our combination of PTOCT and GNR technologies is an attempt to enhance the images acquired via this modality by detecting clinically relevant information about the tissue microenvironment in vivo. Our current studies expand on our previous work, which demonstrated the ability of PTOCT to image endogenous melanin and untargeted GNR in the eye by

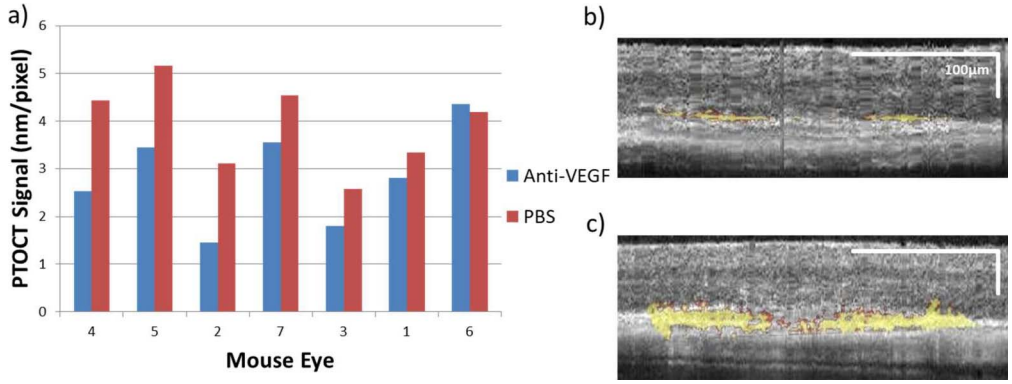

Figure 4. PTOCT of targeted GNR with or without intravitreal anti-VEGF in vivo. (a) PT signal density from every eye in both experimental cohorts, paired by mouse ($n = 7$ mice). The results are ordered from greatest to least magnitude of difference with the horizontal axis numbers matching the eyes to those in Figure 3a. The statistical significance of the difference between the PBS and anti-VEGF eyes was assessed using a Wilcoxon signed-rank test. $W = 27$; $P \leq 0.05$. (b, c) Representative images of OCT b-scans with overlaid lesion-associated photothermal signal, both from mouse 5. Panel (b) shows a lesion from the eye given the anti-VEGF injection, while panel (c) is from the PBS-injected control eye of the same mouse, which shows both a larger lesion and increased PT signal per pixel.

introducing the imaging of ICAM2-targeted GNR, as well as assessing the utility of imaging these targeted GNR to detect pharmacologically induced changes in lesion-associated photothermal signal.[16]

We performed PTOCT imaging on mice injected intravenously with PBS, untargeted GNR, or targeted GNR. We were able to detect the accumulation of both untargeted and ICAM2-targeted GNR in lesions of anatomic laser damage at concentrations significantly different from retinal background. While there is no significant difference between the lesion-associated PT signals from the untargeted versus targeted GNR, there is a trend toward a stronger signal from the targeted group that is consistent with a targeting effect, although further study will be required to confirm this. Given the large standard deviations of the reported measurements in the experimental arms, it is likely that larger sample sizes will be required in future studies. These large standard deviations are likely due to the inherent variability of lesion composition and morphology in the LCNV model.

Our data also suggest that at least a considerable proportion of the observed targeted GNR accumulation occurred due to a targeting-independent mechanism similar to what was observed in our untargeted GNR cohort. Some of this targeting-independent accumulation is likely due to our choice of an 8-hour imaging time point, which is the only time point we have studied thus far. The precise mechanism of this accumulation has not been illuminated for nanoparticles of this size, particularly as it relates PTOCT studies where the nanoparticles must be relatively immobilized to generate a detectable signal.[51] However, these results are consistent with untargeted GNR accumulation shown in our previous study.[16] It has been shown using fluorescein angiography that rodent lesions are at their leakiest 4 to 7 days after lasering.[52] Our studies were all conducted 5 days after lasering. Studies of the altered hemodynamics of rodent LCNV demonstrate that at least by 14 days after lasering there is blood flow through the neovasculature of the lesion, although it is sluggish.[53] There is some evidence that nanoparticles greater than 5 nm in diameter can leak into extravascular space in primate lesions at this time point.[54] Examining this evidence, it is likely that the large target-independent accumulation of GNR in rodent lesions of anatomic laser damage demonstrated in this study are the result of an enhanced permeability and retention (EPR) effect secondary to hemostasis and vascular leakiness, and this effect is likely dependent on the imaging time point.

Additionally, we tested the utility of PTOCT imaging of ICAM2-targeted GNR for detecting changes associated with intravitreal anti-VEGF injections. These injections mimic a clinical intervention common in the treatment of certain retinal vascular diseases, including "wet" AMD, for which LCNV serves as an experimental model. The efficacy of the anti-VEGF injections used in this study was demonstrated by the change in lesion diameter in anti-VEGF versus PBS-injected cohorts. So, this study assessed the ability of PTOCT imaging of ICAM2-targeted GNR to track clinically relevant changes in the severity of retinal vascular disease. However, the changes in PTOCT signal are likely due to passive GNR accumulation, rather than ICAM2 expression. In a clinical setting these changes could be associated with disease progression or with effective treatment. Our results show that PTOCT can detect anti-VEGF induced lesion changes, which indicates that this method may have translational utility for retinal imaging.

The most difficult challenge associated with PTOCT imaging of the retina is the strong PT signal generated by the RPE, which risks overwhelming the signal generated by GNR as well as any targeting effect on GNR delivery. We minimize this problem in our study by only measuring PT signal in the lesions of anatomic laser damage themselves. However, moving forward we will begin to address this limitation with technological changes to GNR targeting and PTOCT imaging. Moving our imaging window further into the near-infrared region would theoretically reduce the amount of light absorbed by melanin in the RPE, which would reduce its PT signal. Higher laser chopping speeds would reduce heat dispersion and along with improvements to the axial resolution of our imaging system could allow for more precise localization of PT signals. Faster imaging times will allow for the imaging of multiple lesions per mouse eye, greatly increasing achievable study power. Different biomarker selections and imaging time points will allow us to optimize our studies for the detection of targeted versus untargeted GNR. PTOCT imaging of GNR in the retina in vivo could allow for faster testing and validation of these novel GNR constructs, helping move GNR technology toward clinical translation. Improved image processing algorithms will directly enhance our ability to separate endogenous from exogenous photothermal signal. Future iterations of these improvements could converge to allow for the generation of images

containing information about absorption of multiple wavelengths of light in relevant tissue, which could differentiate PT signal of the RPE from that of exogenous GNR without the need for processing algorithms or lesion selections.

Conclusion

Our results indicate that PTOCT of GNR is a promising approach for ocular imaging of treatment response. Our unique approach allowed us to maintain the high-resolution structural retinal imaging characteristic of an OCT system while collecting additional information about the retinal tissue microenvironment. We detected clinically relevant reductions in ICAM2-targeted GNR accumulation in the retina following anti-VEGF injection, thus providing feasibility for future studies of molecular expression associated with retinal disease progression. This molecular information could allow for earlier therapeutic intervention in relevant patient populations, leading to improved patient outcomes in those suffering from sight threatening diseases.

Acknowledgments

We thank our colleagues in the Vanderbilt Department of Biostatistics for their assistance with calculating the statistical significance of our data. We also thank Jason Craft and Imam Uddin for help with animal anesthesia and lasering.

Supported by NIH/NEI R01 EY023639, R01 EY023397, R01 EY07533 (JSP), and T32 EY007135, The Carl Marshall Reeves & Mildred Almen Reeves Foundation, Inc., and an Unrestricted Grant from Research to Prevent Blindness, Inc. (JSP).

Disclosure: **A.Y. Gordon**, None; **M. Lapierre-Landry**, None; **M.C. Skala**, None; **J.S. Penn**, None

References

1. Huang D, Swanson EA, Lin CP, et al. Optical coherence tomography. *Science*. 1991;254:1178–1181.
2. Pierro L, Rabiolo A. Emerging issues for optical coherence tomography. *Dev Ophthalmol*. 2017;60:28–37.
3. Schmidt-Erfurth U, Klimshca S, Waldstein SM, Bogunovicb H. A view of the current and future role of optical coherence tomography in the management of age-related macular degeneration. *Eye (Lond)*. 2017;31:26–44.
4. De Barros Garcia JMB, Isaac DLC, Avila M. Diabetic retinopathy and OCT angiography: clinical findings and future perspectives. *Int J Retin Vitr*. 2017; 3.
5. Hood DC. Improving our understanding, and detection, of glaucomatous damage: an approach based upon optical coherence tomography (OCT). *Prog Retin Eye Res*. 2017;57:46–75.
6. Zysk AM, Nguyen FT, Oldenburg AL, Marks DL, Boppart SA. Optical coherence tomography: a review of clinical development from bench to bedside. *J Biomed Opt*. 2007;12:051403.
7. Midena E, Pilotto E. Emerging insights into pathogenesis. *Dev Ophthalmol*. 2017;60:16–27.
8. Rosenfeld PJ. Optical coherence tomography and the development of antiangiogenic therapies in neovascular age-related macular degeneration. *Invest Ophthalmol Vis Sci*. 2016;57:14–26.
9. Phadikar P, Saxena S, Ruia S, Lai TY, Meyer CH, Eliott D. The potential of spectral domain optical coherence tomography imaging based retinal biomarkers. *Int J Retin Vitr*. 2017; 3.
10. Gordon AY, Jayagopal A. Engineering of nanoscale contrast agents for optical coherence tomography. *J Nanomed Nanotechnol*. 2014; 5.
11. Jia Y, Liu G, Gordon AY, et al. Spectral fractionation detection of gold nanorod contrast agents using optical coherence tomography. *Opt Express*. 2015;23:4212–4225.
12. Sen D, SoRelle ED, Liba O, et al. High-resolution contrast-enhanced optical coherence tomography in mice retinae. *J Biomed Opt*. 2016; 21:066002.
13. Rao KD, Choma MA, Yazdanfar S, Rollins AM, Izatt JA. Molecular contrast in optical coherence tomography by use of a pump-probe technique. *Opt Lett*. 2003;28:340–342.
14. John R, Razaeipoor R, Adie SG, et al. In vivo magnetomotive optical molecular imaging using targeted magnetic nanoprobes. *Proc Natl Acad Sci U S A*. 2010;107:8085–8090.
15. Skala MC, Crow MJ, Wax A, Izatt JA. Photothermal optical coherence tomography of epidermal growth factor receptor in live cells using immunotargeted gold nanospheres. *Nano Lett*. 20008;8:3461–3467.
16. Lapierre-Landry M, Gordon AY, Penn JS, Skala MC. In vivo photothermal optical coherence

tomography of endogenous contrast agents in the eye. *Sci Rep*. 2017;7:9228.
17. Adler DC, Huang SW, Huber R, Fujimoto JG. Photothermal detection of gold nanoparticles using phase-sensitive optical coherence tomography. *Opt Express*. 20008;16:4376–4393.
18. Blackmon RL, Sandhu R, Chapman BS, et al. Imaging extracellular matrix remodeling in vitro by diffusion-sensitive optical coherence tomography. *Biophys J*. 2016;110:1858–1868.
19. Troutman TS, Barton JK, Romanowski M. Optical coherence tomography with plasmon resonant nanorods of gold. *Opt Lett*. 2007;32: 438–1440.
20. Hu M, Chen J, Zhi-Yuan L, et al. Gold nanostructures: engineering their plasmonic properties for biomedical application. *Chem Soc Rev*. 2006;35:1084–1094.
21. Ni W, Kou X, Yang Z, Wang J. Tailoring longitudinal surface plasmon wavelengths, scattering, and absorption cross sections of gold nanorods. *ACS Nano*. 2008;2:677–686.
22. Gomez L, Cebrian V, Martin-Saavedra F, Arruebo M, Vilaboa N, Santamaria J. Stability and biocompatibility of photothermal gold nanorods after lyophilization and sterilization. *Materials Res Bulletin*. 2013;48:4051–4057.
23. Xia X, Yang M, Wang Y, et al. Quantifying the coverage density of poly(ethylene glycol) chains on the surface of gold nanostructures. *ACS Nano*. 2012;6:512–522.
24. Schol D, Fleron M, Greisch JF, et al. Anti-PSMA antibody-coupled gold nanorods detection by optical and electron microscopies. *Micron*. 2013; 50:68–74.
25. Joshi PP, Yoon SJ, Hardin WG, Emelianov S, Sokolov KV. Conjugation of antibodies to gold nanorods through Fc portion: synthesis and molecular specific imaging. *Bioconjugate Chem*. 2013;24:878–888.
26. Jung Y, Relf R, Zeng Y, Wang RK. Three-dimensional high-resolution imaging of gold nanorod uptake in sentinel lymph nodes. *Nano Lett*. 2011;3:2938–2943.
27. Tucker-Schwartz JM, Meyer TA, Patil CA, Duvall CL, Skala MC. In vivo photothermal optical coherence tomography of gold nanorod contrast agents. *Biomed Opt Express*. 2012;11: 2882–2895.
28. Tucker-Schwartz JM, Beavers KR, Sit WW, Shah AT, Duvall CL, Skala MC. In vivo imaging of nanoparticle delivery and tumor microvasculature with multimodal optical coherence tomography. *Biomed Opt Express*. 2014;5:1731–1743.
29. Ryan SJ. The development of an experimental model of subretinal neovascularization in disciform macular degeneration. *Trans Am Ophthalmol Soc*. 1979;77:707–745.
30. Dobi ET, Puliofito CA, Destro M. A new model of experimental choroidal neovascularization in the rat. *Arch Ophthalmol*. 1989;107:264–269.
31. Montezuma SR, Vavvas D, Miller JW. Review of the ocular angiogenesis animal models. *Semin Ophthalmol*. 2009;24:52–61.
32. Grossniklaus HE, Kang SJ, Berglin L. Animal models of choroidal and retinal neovascularization. *Prog Retin Eye Res*. 2010;29:500–519.
33. Liu CH, Wang Z, Sun Y, Chen J. Animal models of ocular angiogenesis: from development to pathologies. *FASEB J*. 2017;31:4665–4681.
34. Tobe T, Ortega S, Luna JD, et al. Targeted disruption of the FGF2 gene does not prevent choroidal neovascularization in a murine model. *Am J Pathol*. 1998;153:1641–1646.
35. Giani A, Thanos A, In Roh M, et al. In vivo evaluations of laser-induced choroidal neovascularization using spectral-domain optical coherence tomography. *Invest Ophthalmol Vis Sci*. 2011;52:3880–3887.
36. Toma HS, Barnett JM, Penn JS, Kim SJ. Improved assessment of laser-induced choroidal neovascularization. *Microvasc Res*. 2010;80:295–302.
37. Staunton DE, Dustin ML, Springer TA. Functional cloning of ICAM-2, a cell adhesion ligand for LFA-1 homologous to ICAM-1. *Nature*. 1989;339:61–64.
38. Li T, Aredo B, Zhang K, et al. Phosphatidylserine (PS) is exposed in choroidal neovascular endothelium: PS-targeting antibodies inhibit choroidal angiogenesis in vivo and ex vivo. *Invest Ophthalmol Vis Sci*. 2015;56:7137–7145.
39. Semkova I, Peters S, Welsandt G, Janicki H, Jordan J, Schraermeyer U. Investigation of laser-induced choroidal neovascularization in the rat. *Invest Ophthalmol Vis Sci*. 2013;44:5349–5354.
40. Krause TA, Alex AF, Engel DR, Kurts C, Eter N. VEGF-production by CCR2-dependent macrophages contributes to laser-induced choroidal neovascularization. *PLoS One*. 2014;9:E94313.
41. Shen WY, Yu MJ, Barry CJ, Constable IJ, Rakoczy PE. Expression of cell adhesion molecules and vascular endothelial growth factor in experimental choroidal neovascularization in the rat. *Br J Ophthalmol*. 1998;82:1063–1071.
42. Sakurai E, Taquchi H, Anand A, et al. Targeted disruption of the CD18 or ICAM-1 gene inhibits

choroidal neovascularization. *Invest Ophthalmol Vis Sci*. 2003;44:2743–2749.
43. Lin M, Hu Y, Chen Y, et al. Impacts of hypoxia-inducible factlor-1 knockout in the retinal pigment epithelium on choroidal neovascularization. *Invest Ophthalmol Vis Sci*. 2012;53:6197–6206.
44. Kwak N, Okamoto N, Wood JM, Campochiaro PA. VEGF is major stimulator in model of choroidal neovascularization. *Invest Ophthalmol Vis Sci*. 2000;41:3158–3164.
45. Campa C, Kasman I, Ye W, Lee WP, Fuh G, Ferrara N. Effects of an anti-VEGF-A monoclonal antibody on laser-induced choroidal neovascularization in mice: optimizing methods to quantify vascular changes. *Invest Ophthalmol Vis Sci*. 2008;49:1178–1183.
46. Sulaiman RS, Merrigan S, Quigley J, et al. A novel small molecule ameliorates ocular neovascularization and synergises with anti-VEGF therapy. *Sci Rep*. 2016; 6.
47. Guizar-Sicairos M, Thurman ST, Fienup JR. Efficient subpixel image registration algorithms. *Opt Lett*. 2008;33:156–158.
48. Kam J, Muranaka K, Yanagi Y, Obata R, Tamaki Y, Shibuya M. Inhibition of choroidal neovascularization by blocking vascular endothelial growth factor receptor tyrosine kinase. *Jpn J Ophthalmol*. 2008;52:91–98.
49. Sulaiman RS, Merrigan S, Quigley J, et al. A novel small molecule ameliorates ocular neovascularization and synergises with anti-VEGF therapy. *Sci Rep*. 2016;6:25509.
50. Park JR, Choi W, Hong HK, et al. Imaging laser-induced choroidal neovascularization in the rodent retina using optical coherence tomography angiography. *Invest Ophthalmol Vis Sci*. 2016;57: OCT331–OCT340.
51. Chhetri RK, Blackmon RL, Wu WC, et al. Probing biological nanotopology via diffusion of weakly constrained plasmonic nanorods with optical coherence tomography. *Proc Natl Acad Sci U S A*. 2014;111:4289–4297.
52. Hoerster R, Muether PS, Vierkotten S, Schroder S, Kirchhof B, Fauser S. In-vivo and ex-vivo characterization of laser-induced choroidal neovascularization variability in mice. *Graefes Arch Clin Exp Ophthalmol*. 2012;250:1579–1586.
53. Asrani S, Zou S, D'Anna S, Phelan A, Goldberg M, Zeimer R. Selective visualization of choroidal neovascular membranes. *Invest Ophthalmol Vis Sci*. 1996;37:1642–1650.
54. Tolentino MJ, Husain D, Theodosiadis P, et al. Angiography of fluoresceinated anti-vascular endothelial growth factor antibody and dextrans in experimental choroidal neovascularization. *Arch Ophthalmol*. 2000;118:78–84.